Highly stable fullerene-based porous molecular crystals with open metal sites

C. Grazia Bezzu[1], Luke A. Burt[1], Charlie J. McMonagle[1], Stephen A. Moggach[1,4]*, Benson M. Kariuki[2], David R. Allan[3], Mark Warren[3] and Neil B. McKeown[1]*

The synthesis of conventional porous crystals involves building a framework using reversible chemical bond formation, which can result in hydrolytic instability. In contrast, porous molecular crystals assemble using only weak intermolecular interac-tions, which generally do not provide the same environmental stability. Here, we report that the simple co-crystallization of a phthalocyanine derivative and a fullerene (C_{60} or C_{70}) forms porous molecular crystals with environmental stability towards high temperature and hot aqueous base or acid. Moreover, by using diamond anvil cells and synchrotron single-crystal measurements, stability towards extreme pressure (>4 GPa) is demonstrated, with the stabilizing fullerene held between two phthalocyanines and the hold tightening at high pressure. Access to open metal centres within the porous molecular co-crystal is demonstrated by in situ crystallographic analysis of the chemisorption of pyridine, oxygen and carbon monoxide. This suggests strategies for the formation of highly stable and potentially functional porous materials using only weak van der Waals intermolecular interactions.

Semergent tability is one of the key properties of a porous material and determines its suitability for application[1]. The construction of porous organic materials, such as metal – organic frameworks (MOFs) and covalent organic frameworks (COFs), relies on the reversible formation of a network of chemical bonds between molecular components. Reversible bond formation is required to allow the correction of defects to provide an ordered structure, but this also limits the chemical stability of the materials, particularly towards strongly hydrolytic environments. An alternative and very direct approach to a crystalline porous material, as it does not involve bond formation, is the crystallization of a molecular component to form a solvated crystal, from which the included solvent is then removed to generate porosity. For most molecular crystals, the removal of included solvent results in structural collapse due to the lack of a stabilizing framework of bonds. However, over the past decade, a growing number of compounds, often cages that can act as preformed pores[4–7], have provided crystals with permanent porosity as demonstrated by gas adsorption[8,9]. Such porous molecular crystals can rival the porosity of conventional framework materials[10,11] while offering ease of construction, solution processability and the potential for simple structural regeneration by recrystallization. Nevertheless, it remains questionable whether the structural stability of these porous molecular crystals will be sufficient for the many practical applications for which emergent porous materials are being proposed[1]. Indeed, to date, only a few porous molecular crystals have demonstrated stability towards environments such as high temperature[4,12–17], strong aqueous acid[17,18] or base[13,18] and none have been reported to survive extreme pressures.

Metal derivatives of octa(2′,6′-diisopropylphenoxy)phthalocyanine [(dipPhO)$_8$PcM] form solvated crystals of cubic symmetry belonging to the *Pn*-3*n* space group (Fig. 1a)[19]. The large unit cell (a ~3.7 nm) contains two cubic assemblies of six phthalocyanine molecules surrounding large solvent-filled voids (>10 nm^3) that are interconnected at each corner through channels of ~0.4 nm in diameter. In addition, there are relatively narrow cavities, ~1.2 nm in diameter, that lie between the hexa-phthalocyanine assemblies. Remarkably, the same phthalocyanine nanoporous crystal (PNC) structure reoccurs for many metal complexes of (dipPhO)$_8$PcM (for example M = Mg, Al, Ti, Mn, Fe, Co, Zn, Ru, In)[20]. In addition, the PNC structure is compatible with a large variation in size, shape, type and number of ligands, which may be placed at either of the two distinct axial sites of the metal that face into the void (v) or cavity (c)[20,21]. As is commonly encountered in molecular crystals containing very large solvent-filled voids, structural collapse occurs rapidly on removal of the solvate crystal from contact with the solvent of recrystallization. Previously, it was established that suitable bidentate ligands, such as 4,4′-bipyridyl (bipy), can act as molecular wall-ties by binding together two metal cations across the cavity to give, for example, PNC[Co – *c*bipy – Co][20]. The enhanced stability provided by the wall-ties allows the removal of included solvent resulting in permanent porosity as demonstrated by nitrogen adsorption. Subsequently, we have found that these wall-tie ligands are lost at moderate temperatures and under acidic conditions. This lack of stability would limit the potential applications of these phthalocyanine unsolvated nanoporous crystals (PUNCs), which would be reliant on access to the diverse functionality of the metal centres provided by their porous structure[22], for example, in biomimetic heterogeneous catalysts[23]. In addition, the bonding of the wall-tie ligand to the metal centre may reduce its reactivity.

Co-crystallization of (dipPhO)$_8$PcM with fullerenes

Within the PNC structure, the cavities between the (dipPhO)$_8$PcM cubic assemblies are defined by the concave aromatic surfaces of two phthalocyanines molecules, hence, they were anticipated to be the perfect size and shape for the 'ball and socket' inclusion of a fullerene molecule[24–26]. Pleasingly, single-crystal X-ray diffraction (scXRD) revealed that fullerenes C_{60} and C_{70} are both incorporated into PNCs by simple co-crystallization (Fig. 1b and c).

[1]EaStCHEM, School of Chemistry, University of Edinburgh, Edinburgh, UK. [2]School of Chemistry, Cardiff University, Cardiff, UK. [3]Diamond Light Source, Didcot, UK. [4]Present address: Centre for Microscopy, Characterisation and Analysis and School of Molecular Sciences, The University of Western Australia (M310), Perth, Western Australia, Australia. *e-mail: stephen.moggach@uwa.edu.au; neil.mckeown@ed.ac.uk

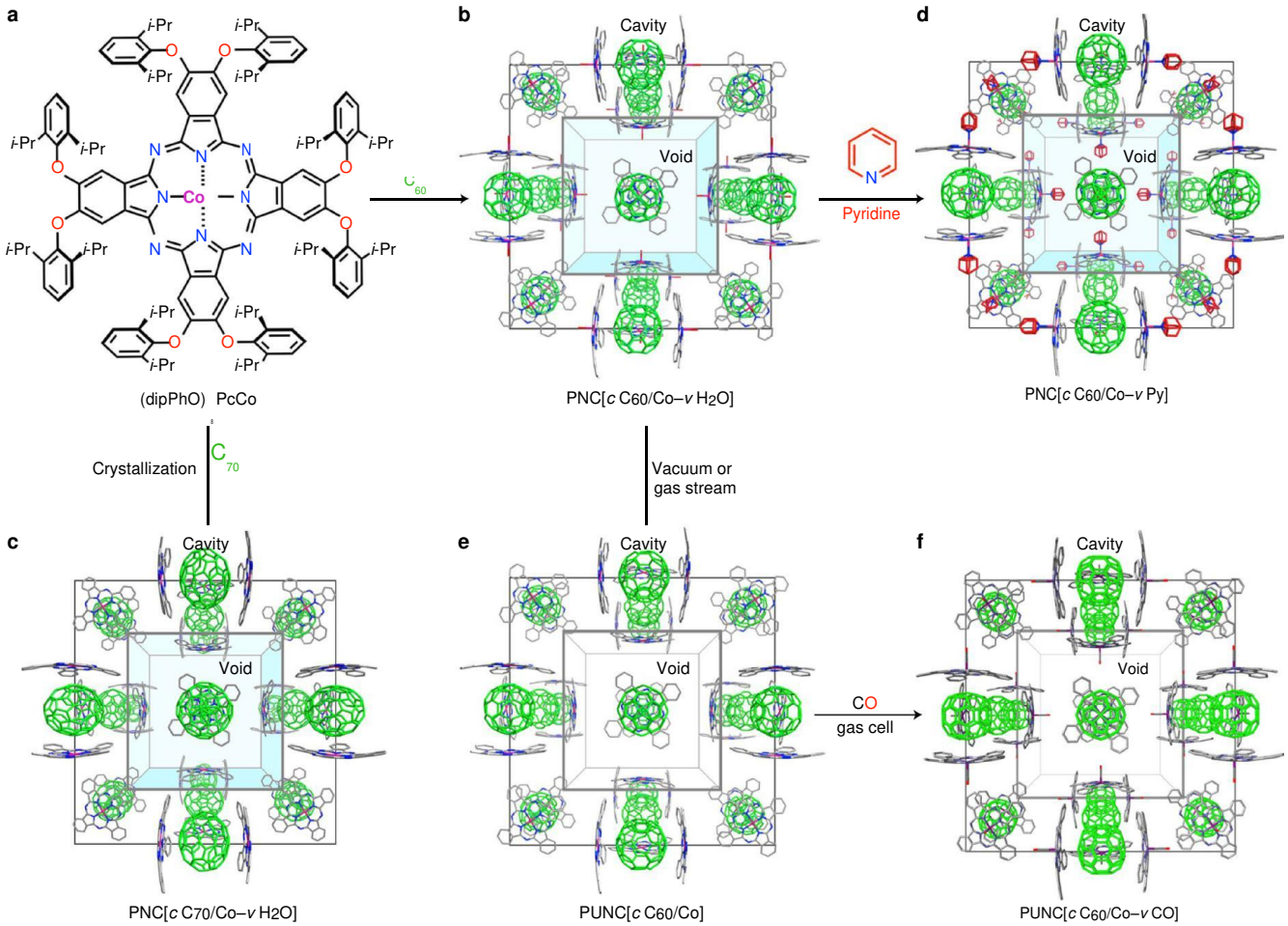

Fig. 1 | The crystal structures of the fullerene-containing PNCs. a, The molecular structure of $(dipPhO)_8PcCo$. **b**,**c**, The fullerene-stabilized PNC[cC$_{60}$/Co–vH$_2$O] (**b**) and PNC[cC$_{70}$/Co–vH$_2$O] (**c**). **d**, The structure of PNC[cC$_{60}$/Co–vPy] obtained from the SCSC exchange of the axial water ligand of PNC[cC$_{60}$/Co–vH$_2$O] for pyridine. **e**,**f**, The structure of unsolvated PUNC[cC$_{60}$/Co] (**e**) and that of PUNC[cC$_{60}$/Co–vCO] (**f**) from the SCSC chemisorption of CO within a gas cell. Note that the eight 2,6-diisopropylphenoxy substituents have been removed from the crystal structures for clarity.

It is notable that previous crystallization studies of $(dipPhO)_8PcCo$ gave a non-porous monoclinic polymorph so that formation of a PNC required the presence of a bulky axial ligand such as pyridine (Py) to give PNC[Co-vPy][21]. However, no added ligand is necessary to obtain PNC[cC$_{60}$/Co – vH$_2$O] or PNC[cC$_{70}$/Co – vH$_2$O], for which adventitious water is bound at the axial site of the Co^{2+} cation and protrudes into the void (Fig. 1b). The strong tendency of fullerenes to encourage PNC crystallization is best illustrated by the formation of PNC[cC$_{60}$/Cu], PNC[cC$_{60}$/Ag] and PNC[cC$_{60}$/H$_2$] from $(dipPhO)_8PcCu$, $(dipPhO)_8PcAg$ and metal-free $(dipPhO)_8PcH_2$, respectively. These complexes had previously yielded only dense non-cubic polymorphs due to the absence of axial ligands, however, the supramolecular binding of the fullerene appears to fulfil a similar role to that of the ligand in blocking one face of the phtha-locyanine and encouraging PNC formation. Hence, fullerene incor-poration increases the elemental diversity that can be incorporated into the PNC system.

Despite the fullerenes fully occupying the cavities, the accessibility of small molecules to the reactive metal centres, via the 0.4 nm channels between the voids, was demonstrated by the single-crystal-to-single-crystal (SCSC) exchange of water for pyri-dine at the Co^{2+} axial site to give PNC[cC$_{60}$/Co – vPy] (Fig. 1d). Access to the other axial site facing into the cavity is blocked by the presence of the fullerene, thereby enforcing penta-coordination at the cobalt. For stability studies, fullerene-based PNCs derived from $(dipPhO)_8PcCo$ were prepared to allow direct comparison with the wall-tie-stabilized PNC[Co-$c$bipy-Co][20].

Structural stability at high pressure

The structural stability of MOFs has been assessed by the pressure at which loss of crystallinity occurs (that is, amorphization), which can help to determine their suitability for potential applications that involve high-pressure environments and mechanical distortion[27,28]. Hence, to compare their structural stability, single crystals of PNC[Co – vPy][20], PNC[Co – $c$bipy – Co][20], PNC[cC$_{60}$/Co – vH$_2$O] and PNC[cC$_{70}$/Co – vH$_2$O] were each subjected to high pressure within a diamond anvil cell using methanol as the hydrostatic liquid. The pressure-induced change in crystal structure was investigated using synchrotron scXRD. The reduction in unit cell volume of each crystal on increasing pressure is shown in Fig. 2a. Diffraction from PNC[Co – vPy] became weak on immediate application of pressure and only unit cell data could be obtained with the crystal dissolv-ing in the hydrostatic liquid at ~2 GPa. Some stabilization due to the bipy wall-tie was apparent for PNC[Co – $c$bipy – Co] with high-quality diffraction data obtained up to 1.0 GPa, followed by a sud-den drop in resolution (from 1.0 – 1.5 Å) with full amorphization complete above 3.0 GPa. The reduction in unit cell volume of 4.2% observed for PNC[Co – $c$bipy – Co] up to 1.0 GPa is predominantly

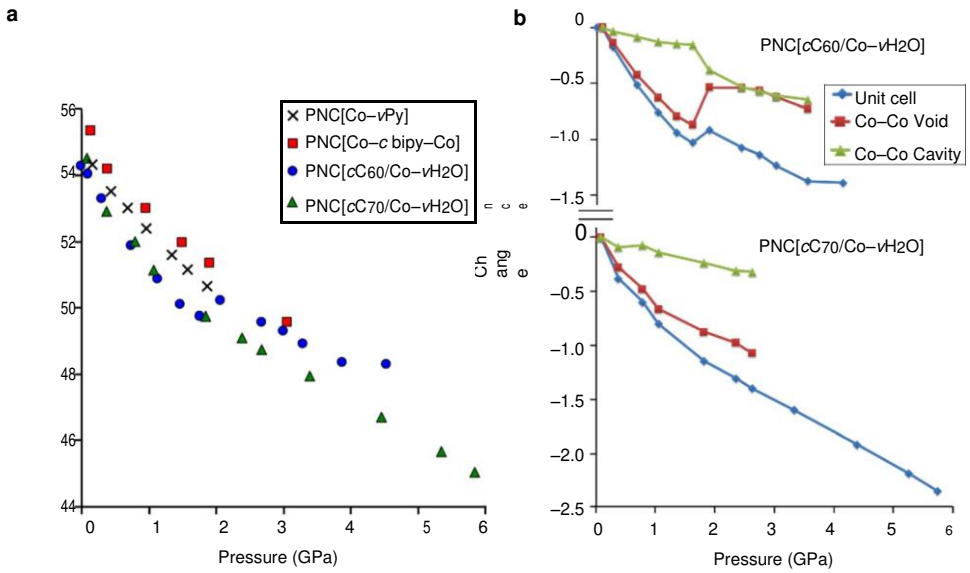

Fig. 2 | Pressure-induced changes in crystal structure. a, Change in unit cell volume on increasing pressure for PNC[Co–*v*Py], PNC[Co–*c*bipy–Co], PNC[*c*C60/Co–*v*H2O] and PNC[*c*C70/Co–*v*H2O]. **b**, Change in Co–Co distances both across the void and fullerene-containing cavity within PNC[*c*C60/ Co–*v*H2O] and PNC[*c*C70/Co–*v*H2O].

due to a significant shortening of the weak bipy N – Co coordinate bond length from 2.418(12) to 2.231(15) Å. Remarkably high stability was evident for both PNC[*c*C60/Co – *v*H2O] and PNC[*c*C70/Co – *v*H2O], which allowed good quality diffraction data to be obtained up to 3.9 and 2.7 GPa, respectively, providing atomic-scale resolution. The stabilizing effect of the fullerenes resulted in amorphization of PNC[*c*C60/Co – *v*H2O] and PNC[*c*C70/Co – *v*H2O] occurring above 4.5 and 5.9 GPa, respectively—values that are higher than those obtained for most rigid MOFs (for example, MOF-5 (ref. 29), ZIF-4 (ref. 30), ZIF-8 (ref. 31), UiO-67 (ref. 32) and Sc_2BDC_3 (ref. 33)), and similar to those that are the most stable (for example, HKUST-1 (ref. 34) and UiO-abdc (ref. 32)). Both fullerene-stabilized PNCs proved highly compressible with the reduction in volume of PNC[*c*C60/Co – *v*H2O] being 11.0% at 4.5 GPa and that of PNC[*c*C70/Co – *v*H2O] being 17.4% at 5.9 GPa.

Uniquely, PNC[*c*C60/Co – *v*H2O] shows an unusual expansion of its unit cell between 1.8 and 2.1 GPa. The good quality scXRD data obtained from high-pressure studies of PNC[*c*C60/Co – *v*H2O] and PNC[*c*C70/Co – *v*H2O] enabled the induced structural changes within the crystals to be determined. Key structural parameters are the Co – Co distances across the solvent-filled void and across the fullerene-containing cavity (Fig. 2b). For both PNC[*c*C60/Co – *v*H2O] up to 1.8 GPa and PNC[*c*C70/Co – *v*H2O] up to 2.6 GPa the reduction in unit cell volume is predominately related to the shrinkage of the void, that is, by compression of the volume of the hexa-phthalocyanine assembly, whereas the size of the fullerene-filled cavity is only slightly compressed. However, for PNC[*c*C60/Co – *v*H2O], on increasing the pressure from 1.8 to 2.1 GPa, the sudden expan-sion of the unit cell coincides with re-inflation of the nanovoid (Co – Co distance increases by 0.34 Å), while the distance across the fullerene-containing cavity is reduced sharply (Co – Co distance decreases by 0.24 Å), hence indicating a tighter embrace of C_{60} by its $(dipPhO)_8PcCo$ host. During this transition the conical shape of the $(dipPhO)_8PcCo$ component, which on initial increase of pressure from 0.1 – 1.8 GPa had become more pronounced, becomes significantly flattened (Fig. 3a). The structural transition is also marked by a conformation change in the isopropyl groups so that the methyls withdraw away from the surface of the C_{60} (Fig. 3b) so as to laterally enlarge the cavity and compensate for its reduction in diameter. The structural transition between 1.8 to 2.1 GPa is also reflected in the C_{60} anisotropic displacement parameter (U_{eq}), where a marked increase from 0.26 $Å_2$ to 0.94 $Å_2$ is observed, indicating that the fullerene becomes more disordered and precesses around the laterally enlarged cavity (Fig. 3c). This behaviour is consistent with the inclu-sion of the hydrostatic liquid on increasing pressure, causing the unit cell volume to increase on increasing pressure. A similar expansion of the unit cell on increasing pressure is not observed for PNC[*c*C70/ Co – *v*H2O]. It is notable that at low pressure (0.1 GPa) the cavity Co – Co distance is ~0.19 Å greater within PNC[*c*C70/Co – *v*H2O] than within PNC[*c*C60/Co-*v*H2O], similar to the small difference in the equatorial diameter of C_{70} relative to C_{60}, whereas at high pres-sure (2.7 GPa) the difference is ~0.40 Å greater across the cavity for PNC[*c*C70/Co – *v*H2O] than for PNC[*c*C60/Co – *v*H2O]. This sug-gests that the larger prolate-shaped C_{70} stops the $(dipPhO)_8PcCo$ host from flattening its conical shape and blocks the very close embrace it achieves with the smaller spherical C_{60}, thereby preventing compression of the cavity and the simultaneous expansion of the void and unit cell. Nevertheless, for PNC[*c*C70/Co – *v*H2O] a similar if more gradual conformational shift of the isopropyl groups to that of PNC[*c*C60/Co-*v*H2O] is observed on increasing pressure (Fig. 3b).

Activation, thermal and chemical stability

Solvent removal from the fullerene-stabilized PNC[*c*C60/Co – *v*H2O] to give unsolvated PUNC[*c*C60/Co] (Fig. 1e) was achieved simply by exposing the crystals to a stream of nitrogen gas at room temperature and was confirmed by thermal gravimetric analysis (TGA) (Fig. 4a). The ease of solvent removal is in contrast to the 'activation' process required for the more hydrophilic MOFs and COFs for which far harsher conditions are usually necessary to obtain the evacuated form of the crystals[35]. Analysis by in situ scXRD, following exposure to a vacuum in the controlled environment of a gas cell, confirms that both the inclusion of C_{60} and C_{70} stabilize the PNC towards solvent removal. A reduction in the Co – Co distance across the cavity (12.74 to 12.44 Å) following solvent removal from PNC[*c*C60/Co – *v*H2O] is presumably related to the accompanying loss of the H_2O axial ligand, which pulls the metal into the void within the solvated crystal. The density of the evacuated crystals is 0.87 g ml^{-1}. A volumetric nitrogen (N_2) adsorption isotherm of PUNC[*c*C60/Co] collected at 77 K (Fig. 4b) confirmed that C_{60} stabilization provides permanent porosity similar to that achieved

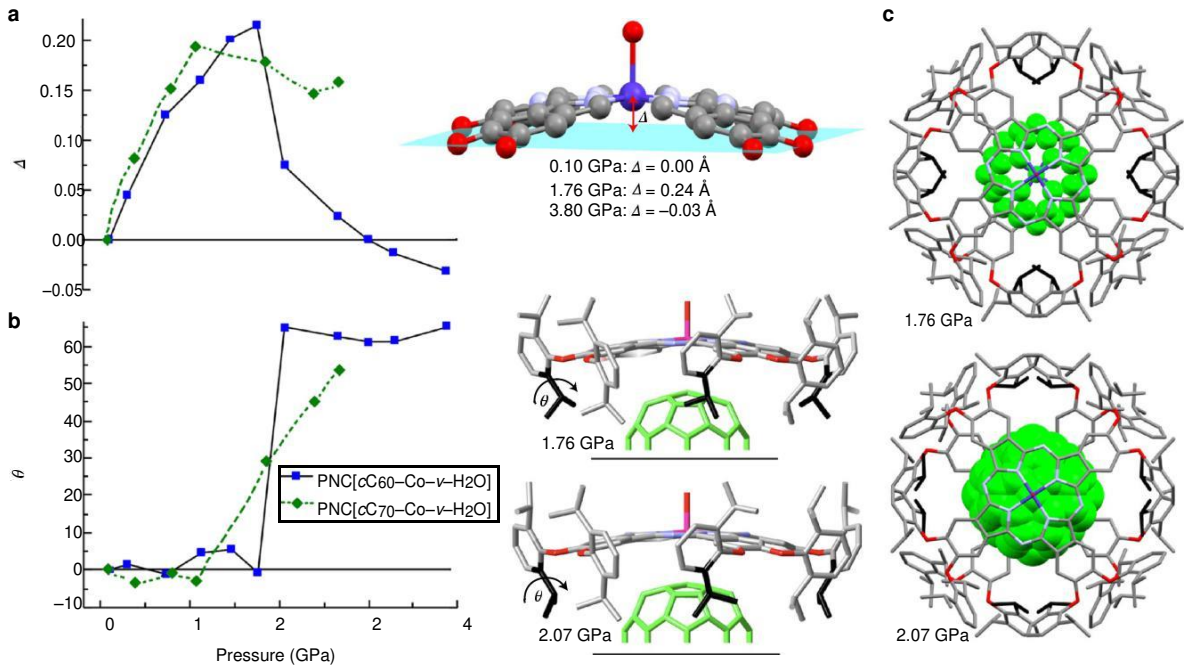

Fig. 3 | Changes in molecular structure of the (dipPhO)$_8$PcCo component on compression of PNC[*c*C$_{60}$/Co–*v*H$_2$O] and PNC[*c*C$_{70}$/Co–*v*H$_2$O]. **a**, The change on increasing pressure of the distance, , between the Co atom and the mean position of the plane containing the eight O atoms on the periphery of the phthalocyanine. The substituents are removed for clarity. **b**, The change in the torsion angle, θ, of the isopropyl groups, shaded black (right), which undergo conformation rearrangement during the structural transformation of PNC[*c*C$_{60}$/Co–*v*H$_2$O] between 1.76 and 2.07 GPa. **c**, A view parallel to the 4 axis (that is, looking down the axial Co–O bond) showing the increase between 1.76 and 2.07 GPa in the C$_{60}$ anisotropic displacement parameters (average U_{eq} value increase from 0.26 Å$_2$ to 0.94 Å$_2$).

using wall-tie ligands[20]. A Brunauer – Emmett – Teller (BET) surface area of 970 m$_2$ g$_{-1}$ and a pore volume of 0.46 ml g$_{-1}$ could be calculated from the isotherm. An inflection point on the low pressure portion of the isotherm is consistent with N_2 adsorption within large micropores as observed previously in molecular crystals containing pores of diameter greater than 1 nm (ref. [6]). A similar clear inflection is observed on the CO_2 isotherm collected at 196 K (Fig. 4b). The pore size distribution calculated from both N_2 and CO_2 isotherms (Supplementary Fig. 1) show that these inflections originate from adsorption within pores of diameter 1.5 – 2.0 nm, consistent with the crystal structure obtained from scXRD.

TGA shows that there is no loss of mass from PUNC[*c*C$_{60}$/ Co] below 700 K, which is the decomposition temperature of the (dipPhO)$_8$PcCo component (Fig. 4a). The thermal stability of PUNC[*c*C$_{60}$/Co] is higher than that of PUNC[Co – *c*bipy – Co] for which mass reduction occurs over the range 350 – 500 K, corresponding to the loss of the bipy wall-tie (~7%) (Fig. 4a). Variable-temperature powder XRD (pXRD) shows that the crystal structure of PUNC[*c*C$_{60}$/Co] is unchanged on heating up to the equipment's maximum accessible temperature of 500 K (Supplementary Fig. 2). Pawley fits of the data for PUNC[*c*C$_{60}$/Co] show the unit cell dimensions smoothly increasing with temperature as would be expected from standard thermal expansion of the crystal (Supplementary Table 1). In contrast, Pawley fits of the analogous pXRD data from PUNC[Co – *c*bipy – Co] (Supplementary Fig. 3) show no increase in cell volume over the temperature range 325 – 400 K, presumably due to the gradual loss of bipy on heating (Supplementary Table 2). The full removal of the bipy wall-tie is also associated with an irreversible crystal – crystal transition between 475 – 500 K.

The stability of PUNC[*c*C$_{60}$/Co] towards hydrolytic conditions was confirmed by scXRD following immersion of crystals in water, aqueous 2 M NaOH and aqueous 2 M HCl all at 100 °C for 24 h (Fig. 4c – e and Supplementary Table 3). Few crystalline porous materials would survive such harsh hydrolytic conditions, although a growing number of MOFs are showing increased resistance to hydrolysis[36–38]. The remarkable thermal, chemical and mechanical stability of the fullerene-stabilized PNCs results from only weak non-covalent interactions, which provide structural resilience due to the very large surface area of intermolecular contact. Although it may appear counterintuitive to use only non-covalent interactions in the design of stable porous organic materials, such interactions between non-polar components will not be disrupted by exposure to a strongly hydrolytic environment.

Chemisorption of CO and O_2 within crystals

The stability of PUNC[*c*C$_{60}$/Co] towards high vacuum (1 × 10$_{-9}$ bar) facilitated the in situ investigation of the chemisorption of CO and O_2 using a gas cell in conjunction with synchrotron scXRD analysis. The open axial site of the Co$_{2+}$ cation that faces into the nanovoid proved to be fully vacant following exposure to high vacuum at room temperature. Incremental dosing of the gas cell with CO at 180 K showed that the axial site was fully occupied at a pressure of 1 bar to give PUNC[*c*C$_{60}$/Co – *v*CO] (Fig. 1f). The Co – C – O bond angle is 180° with the Co – C distance of 2.036(8) Å, which are similar to the analogous bond angle of 180° and Co – C distance of 2.14 Å found recently for CO binding at the open metal site of cobalt porphyrin-based MOF (PCN-224Co) at 200 K (ref. [39]). CO isotherms obtained from PUNC[*c*C$_{60}$/Co] at 196 K show significant uptake at very low pressure consistent with chemisorption (Fig. 4b inset), with sufficient CO adsorbed at 0.2 bar to saturate all Co centres (~10 cc/STP). The isotherms obtained at 196 and 273 K are very similar in shape to those obtained from PCN-224Co and an estimate of the initial heat of adsorption of CO using a dual-site Langmuir–Freundlich model are similar (22 kJ mol^{-1})[39]. O_2 binding within PUNC[*c*C$_{60}$/ Co – *v*O$_2$] proved weaker with a maximum 70.7% occupancy of the axial site obtained at 8.1 bar and 180 K. the Co – O – O bond angle is 145(1)° and the Co – O distance is 2.066(16) Å. These val-ues differ from those of 121° and 1.83 Å, respectively, obtained from

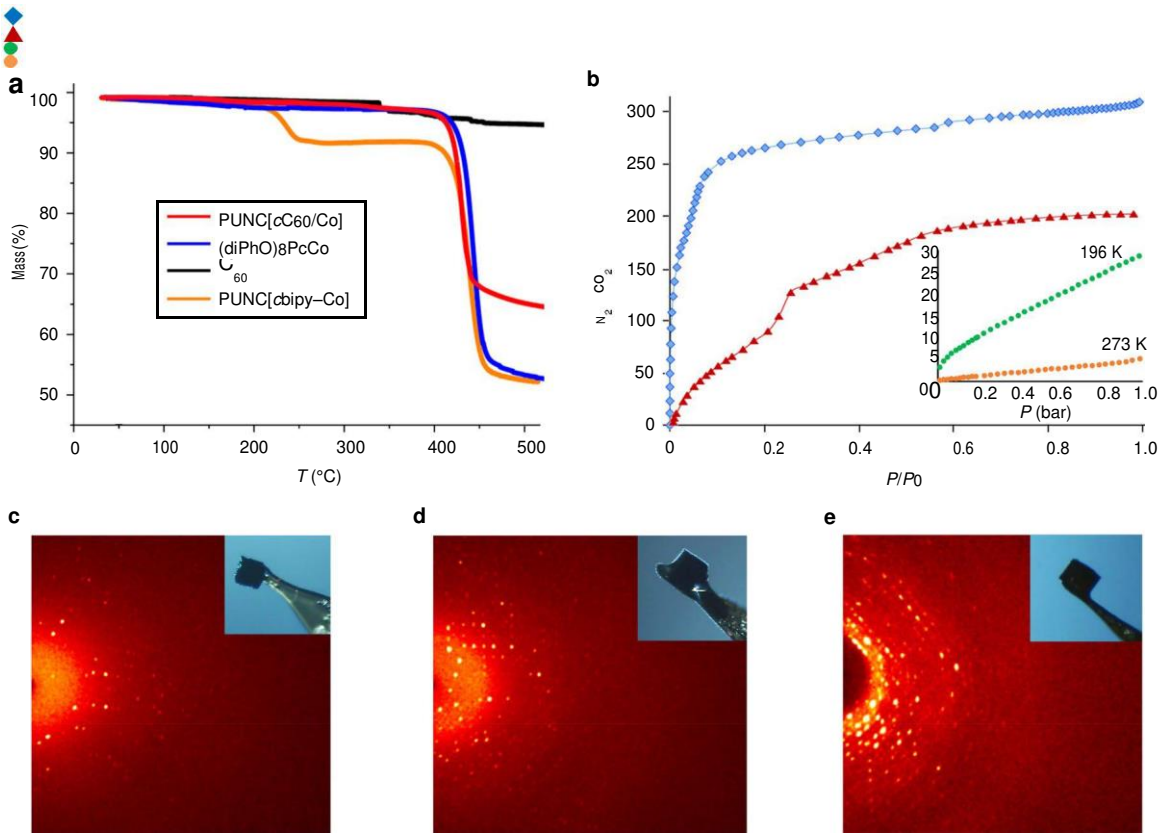

Fig. 4 | Thermal, gas adsorption and XRD data supporting the stability of PUNC[*c*C60/Co]. **a**, Thermal gravimetric analysis of PUNC[*c*C60/Co], PUNC[Co–*c*bipy–Co], (diPhO)8PcCo and C60 demonstrating the greater thermal stability of PUNC[*c*C60/Co] relative to PUNC[Co–*c*bipy–Co], with the latter losing its bipy ligand at ~200 °C. **b**, Adsorption isotherms of PUNC[*c*C60/Co outgassed under vacuum at 125 °C for 2 h: for N_2 (◆blue diamonds) at 77 K, CO_2 (red triangles▲) at 196 K (inset) CO at 196 K (●green circles) and 273 K (●orange circles); desorption data follow closely that of adsorption. STP, standard temperature and pressure. **c**–**e**, Diffraction images of a single crystal (micrograph inset) of PUNC[*c*C60/Co] after soaking in boiling water for 24 h (**c**), boiling aqueous 2 M NaOH for 24 h (**d**), and boiling aqueous 2 M HCl for 24 h (**e**); note that broadening of the diffraction spots is ascribed to fracture of the crystal rather than loss of order.

PCN-224Co, probably due to the much lower temperature of 85 K used during the analysis of O_2 binding within the MOF[40]. Similar studies using PUNC[Co – *c*bipy – Co] demonstrated that the Co^{2+} was unreactive towards O_2 or CO, presumably due to the additional binding of the 4,4′-bipyridyl wall-tie to the metal centre, whereas for PUNC[*c*C60/Co] the metal possesses an open axial binding site.

Outlook

Despite the recognition soon after their discovery of the potential of the fullerenes as components for the synthesis of porous materials[41], to date, attempts to engineer their incorporation into the frame-work of crystals with permanent porosity have not been success-ful. For example, it was anticipated that the commonly encountered porphyrin – fullerene supramolecular motif[42–44] could be used as a 'stabilizing pillar' within porphyrin-based coordination frame-works, however, structural resilience to the removal of the included solvent was not achieved[45–47]. Recently, fullerene-based multidentate ligands were used as building blocks for 2D and 3D coordination frameworks, but these materials also failed to demonstrate stabil-ity towards solvent removal[48–50]. In addition to providing porous materials with exceptional stability, the incorporation of fullerene into PNCs provides intimate contact between the most studied class of photoelectron acceptor (fullerenes) and one of the most studied class of photoelectron donor (phthalocyanines)[51–53]. The ease of combination of these highly functional molecular compo-nents within a porous crystalline material suggests applications as materials for light harvesting, photovoltaics and photocatalysis, for which the environmental and chemical stability demonstrated in this study will be beneficial.

Online content

Any methods, additional references, Nature Research reporting summaries, source data, statements of code and data availability and associated accession codes are available at.

References

\1.\Slater, A. G. & Cooper, A. I. Function-led design of porous materials. *Science* **348**, aaa8075 (2015).

\2.\Furukawa, H., Cordova, K. E., O'Kee e, M. & Yaghi, O. M. e chemistry and applications of metal-organic frameworks. *Science* **341**, 1230444 (2013).

\3.\ Feng, X., Ding, X. S. & Jiang, D. L. Covalent organic frameworks. *Chem. Soc. Rev.* **41**, 6010 – 6022 (2012).

\4.\Jones, J. T. A. et al. Modular and predictable assembly of porous organic molecular crystals. *Nature* **474**, 367 – 371 (2011).

\5.\ McKeown, N. B. Molecular nanoporous crystals: predictable porosity. *Nat. Mater.* **10**, 563 – 564 (2011).

\6.\Zhang, G., Presly, O., White, F., Oppel, I. M. & Mastalerz, M. A permanent mesoporous organic cage with an exceptionally high surface area. *Angew. Chem. Int. Ed.* **53**, 1516 – 1520 (2014).

\7.\Hasell, T. & Cooper, A. I. Porous organic cages: soluble, modular and molecular pores. *Nat. Rev. Mater.* **1**, 16053 (2016).
\8.\McKeown, N. B. Nanoporous molecular crystals. *J. Mater. Chem.* **20**, 10588 – 10597 (2010).
\9.\ Holst, J. R., Trewin, A. & Cooper, A. I. Porous organic molecules. *Nat. Chem.* **2**, 915 – 920 (2010).
\10.\Mastalerz, M. & Oppel, I. M. Rational construction of an extrinsic porous molecular crystal with an extraordinary high speci c surface area. *Angew. Chem. Int. Ed.* **51**, 5252 – 5255 (2012).
\11.\Pulido, A. et al. Functional materials discovery using energy – structure – function maps. *Nature* **543**, 657 – 664 (2017).
\12.\Lim, S. et al. Cucurbit[6]uril: organic molecular porous material with permanent porosity, exceptional stability, and acetylene sorption properties. *Angew. Chem. Int. Ed.* **47**, 3352 – 3355 (2008).
\13.\Chen, T.-H. et al. ermally robust and porous noncovalent organic framework with high a nity for uorocarbons and CFCs. *Nat. Commun.* **5**, 5131 (2014).
\14.\Lee, N. H. et al. A molecular porous zirconium – organic material exhibiting highly selective CO_2 adsorption, high thermal stability, reversible hydration, facile ligand exchange and exclusive dimerization of phenylacetylene. *CrystEngComm* **16**, 5619 – 5626 (2014).
\15.\Nugent, P. S. et al. A robust molecular porous material with high CO_2 uptake and selectivity. *J. Am. Chem. Soc.* **135**, 10950 – 10953 (2013).
\16.\Hu, F. et al. An ultrastable and easily regenerated hydrogen-bonded organic molecular framework with permanent porosity. *Angew. Chem. Int. Ed.* **56**, 2101 – 2104 (2017).
\17.\Hisaki, I. et al. Hexaazatriphenylene-based hydrogen-bonded organic framework with permanent porosity and single-crystallinity. *Chem. Eur. J.* **23**, 11611 – 11619 (2017).
\18.\Liu, M. et al. Acid- and base-stable porous organic cages: shape persistence and pH stability via post-synthetic "tying" of a exible amine cage. *J. Am. Chem. Soc.* **136**, 7583 – 7586 (2014).
\19.\McKeown, N. B. et al. A phthalocyanine clathrate of cubic symmetry containing interconnected solvent- lled voids of nanometer dimensions. *Angew. Chem. Int. Ed.* **44**, 7546 – 7549 (2005).
\20.\Bezzu, C. G., Helliwell, M., Warren, J. E., Allan, D. R. & McKeown, N. B. Heme-like coordination chemistry within nanoporous molecular crystals. *Science* **327**, 1627 – 1630 (2010).
\21.\Bezzu, C. G. et al. In-situ coordination chemistry within cobalt-containing phthalocyanine nanoporous crystals. *CrystEngComm* **15**, 1545 – 1550 (2013).
\22.\McKeown, N. B. *Phthalocyanine Materials: Synthesis, Structure and Function* (Cambridge University Press, 1998).
\23.\Hupp, J. T. Crystal engineering: towards arti cial enzymes. *Nat. Chem.* **2**, 432 – 433 (2010).
\24.\Sakaguchi, K.-i et al. Phenothiazine-bridged cyclic porphyrin dimers as high-a nity hosts for fullerenes and linear array of C_{60} in self-assembled porphyrin nanotube. *J. Org. Chem.* **79**, 2980 – 2992 (2014).
\25.\Saegusa, Y. et al. Supramolecular interaction of fullerenes with a curved π-surface of a monomeric quadruply ring-fused porphyrin. *Chem. Eur. J.* **21**, 5302 – 5306 (2015).
\26.\Bredenkotter, B., Henne, S. & Volkmer, D. Nanosized ball joints constructed from C_{60} and tribenzotriquinacene sockets: synthesis, component self-assembly and structural investigations.*Chem. Eur. J.* **13**, 9931 – 9938 (2007).
\27.\Coudert, F. X. Responsive metal-organic frameworks and framework materials: under pressure, taking the heat, in the spotlight, with friends. *Chem. Mater.* **27**, 1905 – 1916 (2015).
\28.\McKellar, S. C. & Moggach, S. A. Structural studies of metal-organic frameworks under high pressure. *Acta Cryst.* **B71**, 587 – 607 (2015).
\29.\Graham, A. J., Allan, D. R., Muszkiewicz, A., Morrison, C. A. & Moggach, S. A. e e ect of high pressure on MOF-5: guest-induced modi cation of pore size and content at high pressure. *Angew. Chem. Int. Ed.* **50**, 11138 – 11141 (2011).
\30.\Bennett, T. D. et al. Reversible pressure-induced amorphization of a zeolitic imidazolate framework (ZIF-4). *Chem. Commun.* **47**, 7983 – 7985 (2011).
\31.\Moggach, S. A., Bennett, T. D. & Cheetham, A. K. e e ect of pressure on ZIF-8: increasing pore size with pressure and the formation of a high-pressure phase at 1.47 GPa. *Angew. Chem. Int. Ed.* **48**, 7087 – 7089 (2009).
\32.\Hobday, C. L. et al. A computational and experimental approach linking disorder, high-pressure behavior, and mechanical properties in UiO frameworks. *Angew. Chem. Int. Ed.* **55**, 2401 – 2405 (2016).
\33.\Graham, A. J. et al. Stabilization of scandium terephthalate MOFs against reversible amorphization and structural phase transition by guest uptake at extreme pressure. *J. Am. Chem. Soc.* **136**, 8606 – 8613 (2014).
\34.\Graham, A. J., Tan, J. C., Allan, D. R. & Moggach, S. A. e e ect of pressure on Cu-btc: framework compression vs. guest inclusion. *Chem. Commun.* **48**, 1535 – 1537 (2012).
\35.\Howarth, A. J. et al. Best practices for the synthesis, activation, and characterization of metal-organic frameworks. *Chem. Mater.* **29**, 26 – 39 (2017).
\36.\Cavka, J. H. et al. A new zirconium inorganic building brick forming metal organic frameworks with exceptional stability. *J. Am. Chem. Soc.* **130**, 13850 – 13851 (2008).
\37.\Feng, D. W. et al. Zirconium-metalloporphyrin PCN-222: mesoporous metal-organic frameworks with ultrahigh stability as biomimetic catalysts. *Angew. Chem. Int. Ed.* **51**, 10307 – 10310 (2012).
\38.\Lv, X. L. et al. A base-resistant metalloporphyrin metal – organic framework for C – H bond halogenation. *J. Am. Chem. Soc.* **139**, 211 – 217 (2017).
\39.\Gallagher, A. T., Malliakas, C. D. & Harris, T. D. CO binding at a four-coordinate cobaltous porphyrin site in a metal-organic framework: structural, EPR, and gas adsorption analysis. *Inorg. Chem.* **56**, 4654 – 4661 (2017).
\40.\Gallagher, A. T. et al. Dioxygen binding at a four-coordinate cobaltous porphyrin site in a metal-organic framework: structural, EPR, and O_2 adsorption analysis. *Inorg. Chem. Frontiers* **3**, 536 – 540 (2016).
\41.\O'Kee e, M. C_{60} zeolites. *Nature* **352**, 674 (1991).
\42.\Bhyrappa, P. & Karunanithi, K. Porphyrin-fullerene, C_{60}, cocrystallates: in uence of C_{60} on the porphyrin ring conformation. *Inorg. Chem.* **49**, 8389 – 8400 (2010).
\43.\Wang, Y. B. & Lin, Z. Y. Supramolecular interactions between fullerenes and porphyrins. *J. Am. Chem. Soc.* **125**, 6072 – 6073 (2003).
\44.\Konarev, D. V., Khasanov, S. S. & Lyubovskaya, R. N. Fullerene complexes with coordination assemblies of metalloporphyrins and metal phthalocyanines. *Coord. Chem. Rev.* **262**, 16 – 36 (2014).
\45.\Taylor, S. K., Jameson, G. B. & Boyd, P. D. W. A new polymeric framework formed by the self assembly of 5,10,15,20-tetra(3-pyridyl)porphyrin, HgI_2 and C_{60}. *Supramol. Chem.* **17**, 543 – 546 (2005).
\46.\Boyd, P. D. W. & Reed, C. A. Fullerene-porphyrin constructs. *Acc. Chem. Res.* **38**, 235 – 242 (2005).
\47.\Sun, D., am, F. S., Reed, C. A. & Boyd, P. D. W. Extending supramolecular fullerene-porphyrin chemistry to pillared metal-organic frameworks. *Proc. Natl Acad. Sci. USA* **99**, 5088 – 5092 (2002).
\48.\Peng, P., Li, F. F., Neti, V., Metta-Magana, A. J. & Echegoyen, L. Design, synthesis, and X-ray crystal structure of a fullerene-linked metal – organic framework. *Angew. Chem. Int. Ed.* **53**, 160 – 163 (2014).
\49.\Kraf, A. et al. ree-dimensional metal-fullerene frameworks. *Chem. Eur. J.* **22**, 5982 – 5987 (2016).
\50.\Rice, A. M., Dolgopolova, E. A. & Shustova, N. B. Fulleretic materials: buckyball- and buckybowl-based crystalline frameworks. *Chem. Mater.* **29**, 7054 – 7061 (2017).
\51.\Ragoussi, M.-E. & Torres, T. Modern synthetic tools toward the preparation of sophisticated phthalocyanine-based photoactive systems. *Chem. Asian J.* **9**, 2676 – 2707 (2014).
\52.\Bottari, G., Trukhina, O., Ince, M. & Torres, T. Towards arti cial photosynthesis: supramolecular, donor – acceptor, porphyrin- and phthalocyanine/carbon nanostructure ensembles. *Coord. Chem. Rev.* **256**, 2453 – 2477 (2012).
\53.\Bottari, G., de la Torre, G., Guldi, D. M. & Torres, T. Covalent and noncovalent phthalocyanine-carbon nanostructure systems: synthesis, photoinduced electron transfer, and application to molecular photovoltaics. *Chem. Rev.* **110**, 6768 – 6816 (2010).

Acknowledgements

We thank the EPSRC via grant EP/N01331X/1 and the University of Edinburgh for funding and the Diamond Light Source for beamtime on Station I19.

Author contributions

C.G.B. prepared the fullerene-based crystals and performed porosity and stability analysis. L.A.B. prepared the silver phthalocyanine and crystals derived from it. C.J.M. collected and analysed crystallographic data at the University of Edinburgh and the DLS, Station I19. S.A.M. designed the high-pressure experiments, collected data, refined the crystallographic structures and supervised the crystallographic analysis of the materials. B.K. collected crystallographic data at the DLS, Station I19. D.R.A. designed DLS Station I19, supervised its operation and helped with data collection and processing. M.W. constructucted the gas cell associated with DLS, Station I19 and helped with data collection and processing. N.B.M. conceived the idea of the incorporation of fullerenes within the phthalocyanine molecular crystals, supervised the synthesis of materials and wrote the manuscript with input from all of the authors.

Competing interests

The authors declare no competing interests.

Additional information

Supplementary information is available for this paper at

.

Methods

Materials. Molecular components $(dipPhO)_8PcCo$ and $(dipPhO)_8PcH_2$ were prepared, puri ed and characterized as previously reported[20]. Commercially available reagents were purchased from Sigma-Aldrich and used without further puri cation. Fullerenes C_{60} (98% purity) and C_{70} (99% purity) were used. Infrared (IR) spectra were recorded in the range 4,000 – 600 cm^{-1} using a Jasco FTIR-660 plus spectrometer. UV – visible absorption spectra were recorded in the range 200 – 800 nm using a Jasco V-570 UV/vis/NIR spectrophotometer. Volumetric N_2 sorption studies were undertaken at 77 K using a Beckman Coulter 3100 Surface Area Analyzer (Fullerton, California, USA) and CO_2 sorption studies were undertaken at 195 K using a Quantachrome NOVA 2000e. ^{1}H NMR spectra were measured in $CDCl_3$ using an Avance Bruker DPX 400 instrument (400 MHz), with ^{13}C NMR spectra recorded at 100 MHz respectively. Matrix-assisted laser desorption ionization-time of ight (MALDI-TOF) mass spectroscopic analyses were performed with a Waters MALDI Micro MX spectrometer.

2,3,9,10,16,17,23,24-octa(2′,6′-diisopropylphenoxy)phthalocyaninatocopper. A solution of $(dipPhO)_8PcH_2$ (0.10 g, 0.05 mmol) and a large excess of Cu(ii)acetate (0.47 g, 2.5 mmol) in dry *n*-pentanol (5 ml) was heated at reflux for 4 h. After cooling, toluene was added to the slurry of reaction that was filtered to remove the excess of Cu(ii)acetate, then the solvent was evaporated under reduced pressure. The crude product was purified by repeated reprecipitation with methanol from its solution in dichloromethane (DCM) to give $(dipPhO)_8PcCu$ as a green solid (0.08 g, 77%). Melting point (m.p.) > 300 °C; IR (film) (cm^{-1}): 2,962, 1,611, 1,461, 1,406, 1,351, 1,271, 1,186, 1,095, 1,034, 899, 797, 775; UV – vis (DCM): λ_{max} 682, 614, 405, 343, 295, 230 nm; MS (MALDI-TOF): cluster centred at mass/charge ratio (*m/z*) 1,988.33(MH^+); elemental analysis calculated (%) for $C_{128}H_{144}N_8O_8Cu$: C 77.41, H 7.31, N 5.64, found C 77.97, H 7.52, N 5.36.

2,3,9,10,16,17,23,24-octa(2′,6′-diisopropylphenoxy)phthalocyaninatosilver. A mixture of $(dipPhO)_8PcH_2$ (0.30 g, 0.16 mmol) and $AgNO_3$ (0.27 g, 1.56 mmol) in dimethylformamide (DMF, 8 ml) was heated to 120 °C for 2 h. The reaction was then poured into water and the solid formed filtered off, washed with water, then methanol and allowed to dry under suction. The crude solid was purified by precipitation from chloroform into methanol to yield 2,3,9,10,16,17,23,24-octa(2′,6′-diisopropylphenoxy)phthalocyaninatosilver as a green solid (0.19 g, 61% mmol). M.p. > 300 °C; IR (solid) (cm^{-1}): 3,064, 2,962, 2,929, 2,868, 1,606, 1,435, 1,382, 1,361, 1,327, 1,180, 1,141, 1,095, 1,024, 993, 935, 900, 858, 792, 773, 736, 721, 516; UV – vis (DCM): λ_{max} 676.4, 611.8, 352.0, 293.6 nm; MS (MALDI-TOF) (*m/z*): calculated 2,030.01, found cluster centred at 2,029.49 (MH_+).

Crystallizations. Compounds $(dipPhO)_8PcH_2$, $(dipPhO)_8PcCu$ and $(dipPhO)_8PcAg$ were crystallized by slow diffusion of methanol into their chloroform solutions. Crystals of PNC[Co – *v*Py] (CCDC761407) and PNC[Co – *c*bipy – Co] (CCDC761419) with pyridine or bipyridine wall-tie, respectively, were obtained as previously reported[20]. PNC[cC$_{60}$/H_2], PNC[cC$_{60}$/Cu], PNC[cC$_{60}$/Ag], PNC[cC$_{60}$/Co – vH$_2$O] and crystals were obtained by slow diffusion of methanol into equimolar toluene solutions of $(dipPhO)_8PcM$ (M = 2H, Cu, Ag, Co) and C_{60}. PNC[cC$_{70}$/Co – vH$_2$] was prepared in the same way from $(dipPhO)_8PcCo$ and C_{70}. Unsolvated PUNC[cC$_{60}$/Co], PUNC[cC$_{60}$/H_2], PUNC[cC$_{60}$/Cu] and PUNC[cC$_{60}$/Ag] were obtained by placing the solvated PNCs under vacuum using the gas cell apparatus described below (see section 'Gas cell experiments'). PNC[cC$_{60}$/Co – vPy] crystals were obtained by adding pyridine into the solvent in contact with the PNC[cC$_{60}$/Co – vH$_2$O] crystals, employing the same method previously used for ligand exchange in PNCs[21]. The purity of unsolvated crystals of PUNC[cC$_{60}$/Co] crystals was confirmed by elemental analysis: calculated (%) for C_{60}@2$C_{128}H_{144}N_8O_8Co$: C 81.04, H 6.20, N 4.79, found C 80.90, H 5.43, N 4.35.

Thermal gravimetric analyses (TGA). Thermogravimetric analysis was performed on a TA SDT Q 600 instrument. The thermal stabilities of C_{60}, $(dipPhO)_8PcCo$ and of the unsolvated crystals of PUNC[cC$_{60}$/Co] and PUNC[Co – *c*bipy – Co] (Fig. 4a) were measured by ramping the temperature at a rate of 10 °C min^{-1}. No mass loss was observed at low temperature (<100 °C), confirming the absence of solvents from the crystals. A mass loss of ~7% starting at ~230 °C was observed for PUNC[Co – *c*bipy – Co] that corresponds to the loss of the bipyridyl ligand. For the three phthalocyanine samples, a mass loss of ~50% starting at ~430 °C, which corresponds to the decomposition temperature of the phthalocyanine, was observed. For the PUNC[cC$_{60}$/Co] crystals, further mass loss was observed starting at ~700 °C, which is due to the thermal decomposition of fullerene.

Gas adsorption and pore size distribution. Volumetric N_2 sorption studies were undertaken at 77 K using a Beckman Coulter 3100 Surface Area Analyzer (Fullerton, California, USA) and CO_2 sorption studies were undertaken at 195 K using a Quantachrome NOVA 2000e. PUNC[cC$_{60}$/Co] crystals were degassed at 150 °C for at least 2 h before measurement (Fig. 4b). Pore size distribution was calculated from the N_2 adsorption isotherm collected at 77 K and the CO_2 adsorption isotherms collected at 195 and 273 K using the slit-shaped pre Haworth – Kawazoe model (Supplementary Fig. 1).

Powder X-ray diffraction. Variable-temperature X-ray powder diffraction data were collected from PUNC[cC$_{60}$/Co] (Supplementary Fig. 2) and PUNC[Co – *c*bipy – Co] (Supplementary Fig. 3) from 293 K to 500 K in approximately 25 K steps. The samples were loaded in glass capillaries, and mounted on a Bruker d8 diffractometer using Cu Kα radiation (λ = 1.54056 Å). Data were collected from 6 to 20° in 2θ. Pawley fits of these data were performed using Topas, in order to extract cell dimensions as a function of temperature (Supplementary Tables 1 and 2).

Chemical stability of PUNC[cC$_{60}$/Co]. The chemical stability in water, acid and base of PUNC[cC$_{60}$/Co] crystals was tested by suspending crystals in MeOH, which was then exchanged with water and the sample heated at 100 °C for 4 h. The same sample was then split into three batches. The water was exchanged with 2 M HCl in one sample and with 2 M NaOH in another, then both were heated at 100 °C for 24 h. The solid from each of the three samples, which looked macroscopically unchanged, was then washed and suspended in MeOH. Crystals were then isolated and indexed using single-crystal X-ray diffraction, collected on a Bruker ApexII diffractometer with graphite-monochromated Mo *K*α radiation (λ = 0.71073 Å) at room temperature (Fig. 4c – e and Supplementary Table 3).

Laboratory single-crystal measurements. Single crystals were mounted onto a MiTiGen Microloops and a sphere of data collected on a Bruker SMART APEX II diffractometer with graphite-monochromated Mo *K*α radiation (λ = 0.71073 Å) at 150 K. These data were integrated using the program SAINT and the absorption correction was carried out using the program SADABS version 2008-1. Tabulated crystallographic information for the non-cubic structures of $(dipPhO)_8PcH_2$ and $(dipPhO)_8PcCu$ are included in Supplementary Table 4 (CCDC 1851707 and 1851708, respectively).

Ambient-pressure low-temperature synchrotron single-crystal measurements. A single crystal of PNC[cC$_{60}$/Co – vPy], and separately, a single crystal of PUNC[cC$_{60}$/Co] (which was de-solvated simply by exposing the crystals to a stream of nitrogen gas at room temperature) were mounted onto a MiTiGen Microloops and a sphere of data collected on a CrystalLogic kappa 3-circle goniometer on station I19 at the Diamond Light Source, Rutherford Appleton Laboratory, on a Rigaku Saturn 724 CCD detector using synchrotron radiation (λ = 0.6889 Å). Data collection was carried out using an exposure time and a step size of 1 s and 1°, respectively. The data were integrated using the program CrystalClear. In a separate experiment, a single crystal of the non-cubic $(dipPhO)_8PcAg$ was placed on a kappa 3-circle goniometer, also on station I19 and data collected using a Pilatus 2M detector. Data collection was carried out using shutterless operation with a step size and time step of 0.5˚ and 0.05 s, respectively. The absorption correction and merging of data were carried out using CrystalClear-SM Expert 2.0 for all datasets (Supplementary Table 5, CCDC1853490, 1857087 and 1856443).

High-pressure crystallographic studies. The high-pressure crystallography was performed according to ref. [54], and reproduced here for completeness. High-pressure single-crystal diffraction experiments were carried out on PNC[Co – *c*bipy – Co], PNC[cC$_{60}$/Co – vH$_2$O], PNC[cC$_{70}$/Co – vH$_2$O] and PNC[Co – vPy] using methanol as a hydrostatic medium (Supplementary Table 6). A single crystal of each of the four compounds was loaded into a Merrill – Bassett diamond anvil cell with a half-opening angle of 40°, composed of Boehlar Almax diamonds with 600 μm cutlet diamond anvils, a tungsten gasket and tungsten carbide backing plates[55]. A small ruby chip was also loaded into the cell to act as a pressure calibrant, using the pressure-dependent fluorescence of the ruby to measure the pressure. Diffraction data were collected on station I19 at the DIAMOND Light Source, Rutherford Appleton Laboratory, on a Rigaku Saturn 724 CCD detector using synchrotron radiation (λ = 0.5159 Å). Data collections were carried out using an exposure time and a step size of 1 s and 0.5°, respectively. The data were integrated using the program SAINT using dynamic masks, these mask the regions of the detector that are shaded due to the pressure cell. Omission of shaded reflections, absorption correction and merging of data were carried out in a three-step process, first with the program SHADE (2004), then SADABS (2008) and finally XPREP (2004). For PNC[Co – *c*bipy – Co], data were collected from 0.14 to 3.06 GPa, for PNC[cC$_{60}$ – Co – vH$_2$O] from 0.10 to 4.53 GPa, for PNC[cC$_{70}$/Co – vH$_2$O] from 0.08 to 5.85 GPa and for PNC[Co – vPy] from 0.16 to 1.87 GPa. Structural refinements are only reported for PNC[Co – *c*bipy – Co] to 0.96 GPa, for PNC[cC$_{60}$/Co – vH$_2$O] to 3.88 GPa and PNC[cC$_{70}$/Co – vH$_2$O] to 2.67 GPa. Above these pressures the samples became polycrystalline. No structural refinements could be obtained for PNC[Co – vPy].

Structure refinements for variable-pressure data. Structure refinements were carried out in CRYSTALS[56]. For PNC[cC$_{60}$/Co – vH$_2$O] (Supplementary Table 7; CCDC1851749 – 1851759), the $(dipPhO)_8PcM$ group was refined anisotropically, while the encapsulated C_{60} was refined isotropically. All structures were refined against *F* (structure factor) with a I/σ cut-off of 2. All 1,2 and 1,3 distances for the organic linker were restrained, while all torsion angles and metal – ligand bond distances were allowed to freely refine. The C_{60} is disordered about the – 4 axis.

The best refinement results were obtained by assigning eight q-peaks within the cavity as C atoms. The 1,2 distances were then restrained to 1.54 Å. Vibrational and thermal similarity restraints were also applied to the organic linker and C_{60}. Hydrogen atoms on the linker were placed geometrically and constrained to ride on their host atoms. The pore volume and electron count per unit cell (and therefore the solvent count) were calculated using the SQUEEZE algorithm in PLATON[57].

For PNC[*c*C_{70}/Co – *v*H_2O] (Supplementary Table 8; CCDC1851729 – 1851735), the data were of low resolution (1.5 Å at best). Nevertheless, a model for the included C_{70} was obtained in a similar fashion to C_{60}, with the best refinement results obtained by assigning nine q-peaks within the cavity as C atoms. The 1,2 distances were then restrained to 1.54 Å with rather 'loose' restraints. Vibrational and thermal similarity restraints were also applied to the organic linker and C_{70}. From 0.08 to 2.67 GPa, the conformation of the (dipPhO)$_8$PcM group and the C_{70} were refined against *F* with a I/σ cut-off of 2, while the included solvent was modelled using the SQUEEZE algorithm in PLATON. All 1,2 and 1,3 distances for the organic linker were restrained while all torsion angles and metal – ligand bond distances were allowed to freely refine. Vibrational and thermal similarity restraints were also applied to the organic linker. Hydrogen atoms on the linker were placed geometrically and constrained to ride on their host atoms. The pore volumes were calculated using the SQUEEZE algorithm in PLATON[57].

For PNC[Co – *c*bipy – Co] (Supplementary Table 9; CCDC1851743 – 1851745), the (dipPhO)$_8$PcM group was refined anisotropically, along with the bound bipy and axial pyridine ligand, which were disordered about the −4 axis. All structures were refined against *F* with a I/σ cut-off of 2. All 1,2 and 1,3 distances for the organic linkers were restrained, while all torsion angles and metal – ligand bond distances were allowed to freely refine.

For PNC[Co – *v*Py] only unit cell dimensions are reported (Supplementary Table 10).

Gas cell experiments. Gas cell experiments were carried out on station I19 using a quartz capillary static cell with a 5 mm outer diameter. The cell was attached to a goniometer head containing a standard Mitegen mount in which crystals of PUNC[*c*C_{60}/Co], PUNC[*c*C_{60}/H_2], PUNC[*c*C_{60}/Ag] and PUNC[*c*C_{60}/Cu] were glued in order to avoid sample movement on application of pressure. The goniometer head was then connected to a gas rig though stainless steel capillary tubing (Swagelok SS-T1-S-014-6ME). Data were collected for PUNC[*c*C_{60}/ Co] from high-vacuum (for at least 20 min, vacuum = 10^{-6} mbar) to 6.4 bar in CO (Supplementary Table 11; CCDC1851736 – 1851742) and 8.5 bar in O_2 (Supplementary Table 12; CCDC1851416 – 1851422). After exposing PUNC[*c*C_{60}/ Co] to CO, the crystal was then evacuated for at least 10 min to ascertain the reversibility of gas uptake in the pores. For PUNC[*c*C_{60}/Cu], PUNC[*c*C_{60}/Ag] and PUNC[*c*C_{60}/H_2] (Supplementary Table 13; CCDC1851746 – 1851748), the gas cell was used to collect fully evacuated crystals held under high vacuum, in order to remove as much solvent as possible, though a very small amount of residual electron density could still be seen in the pores, the axial water ligand was removed successfully. Data collections were carried out using an exposure time and a step size of 1 s and 0.5°, respectively, using a Pilatus 300K photon-counting pixel array detector. For each dataset, a full sphere of data was collected. Data processing was carried out using the program xia2[58], while the adsorption correction was carried out using the program SCALA[59,60].

Structure refinements were carried out in CRYSTALS[56]. All structures were refined against *F* with a I/σ cut-off of 2. All 1,2 and 1,3 distances for the organic linker and C_{60} were restrained, while all torsion angles and metal – ligand bond distances were allowed to freely refine. Vibrational and thermal similarity restraints were also applied to the organic linker and C $_{60}$. Hydrogen atoms on the linker were placed geometrically and constrained to ride on their host atoms. The pore volume and electron count per unit cell (and therefore the adsorbed gas content) were calculated using the SQUEEZE algorithm in PLATON[57].

Data avaliability

Crystallographic data are available free of charge from the Cambridge Crystallographic Data Centre (CCDC) http://www.ccdc.cam.ac.uk/data_request/cif by using the following deposition codes. CCDC1851707: non cubic form of (dipPhO)$_8$PcH_2 (Supplementary Table 4); CCDC1851708: non cubic form of (dipPhO)$_8$PcCu (Supplementary Table 4); CCDC1853490: PNC[*c*C_{60}/Co – *v*Py] (Supplementary Table 5) CCDC1856443: non-cubic form of (dipPhO)$_8$PcAg (Supplementary Table 5); CCDC1857087: PUNC[*c*C_{60}/Co] desolvated by stream of nitrogen at room temperature (Supplementary Table 5); CCDC1851749 – 1851759: PNC[*c*C_{60}/Co – *v*H_2O] high-pressure compression study (Supplementary Table 7); CCDC185729 – 1851735: PNC[*c*C_{70}/Co – *v*H_2O] high-pressure compression study (Supplementary Table 8); CCDC1851743 – 1851745: PNC[Co – *c*bipy – Co] high-pressure compression study (Supplementary Table 9); CCDC1851736 – 1851742: structures of PUNC[*c*C_{60}/Co] from gas cell experiments including structure evacuated in vacuum and subjected up to 8.5 bar of CO (Supplementary Table 11); CCDC1851416 – 1851422: structures of PUNC[*c*C_{60}/Co] from gas cell experiments including structure evacuated in vacuum and subjected up to 8.5 bar of O_2 (Supplementary Table 12); CCDC1851746: PUNC[*c*C_{60}/Cu] desolvated by application of vacuum in gas cell (Supplementary Table 13); CCDC1851747: PUNC[*c*C $_{60}$/Ag] desolvated by application of vacuum in gas cell (Supplementary Table 13); CCDC1851748: PUNC[*c*C_{60}/H_2] desolvated by application of vacuum in gas cell (Supplementary Table 13).

References

\54.\McKellar, S. C. et al. Pore shape modi cation of a microporous metal – organic framework using high pressure: accessing a new phase with oversized guest molecules. *Chem. Mater.* **28**, 466 – 473 (2016).

\55.\Moggach, S. A., Allan, D. R., Parsons, S. & Warren, J. E. Incorporation of a new design of backing seat and anvil in a Merrill-Bassett diamond anvil cell. *J. Appl. Crystal.* **41**, 249 – 251 (2008).

\56.\Betteridge, P. W., Carruthers, J. R., Cooper, R. I., Prout, K. & Watkin, D. J. CRYSTALS version 12: sofware for guided crystal structure analysis. *J. Appl. Crystal.* **36**, 1487 (2003).

\57.\Spek, A. L. Single-crystal structure validation with the program PLATON. *J. Appl. Crystal.* **36**, 7 – 13 (2003).

\58.\Winter, G. xia2: an expert system for macromolecular crystallography data reduction. *J. Appl. Crystal.* **43**, 186 – 190 (2010).

\59.\Collaborative Computational Project, Number 4 e CCP4 suite: programs for protein crystallography. *Acta Crystal.* **D50**, 760 – 763 (1994).

\60.\Evans, P. Scaling and assessment of data quality. *Acta Crystal.* **D62**, 72 – 82 (2006).